

Equalization in Aeronautical Telemetry Using Multiple Transmit Antennas

MICHAEL RICE, Senior Member, IEEE
Brigham Young University
Provo, UT, USA

MD. SHAH AFRAN
MOHAMMAD SAQUIB, Senior Member, IEEE
The University of Texas at Dallas
Dallas, TX, USA

This paper introduces a generalized time-reversed space-time block code (GTR-STBC) for single-carrier systems employing multiple transmit antennas and operating over frequency-selective multipath fading channels. The generalization involves unequal power allocation parameterized by ρ . The criteria for selecting the optimum ρ is minimizing the postequalizer mean-squared error for a minimum mean-squared error (MMSE) equalizer. GTR-STBC is applied to measured channel impulse responses and a simple statistical channel model. The results show that 1) the optimum value of ρ gives the best trade-off between signal-to-noise ratio and intersymbol interference (ISI); 2) equal power allocation may not be the optimum power allocation when channel state information is available; and 3) the optimum profile of ρ over measured channels is significantly different than from that in statistical channel models.

Manuscript received April 10, 2013; revised December 20, 2014;
released for publication February 23, 2015.

DOI. No. 10.1109/TAES.2015.140289.

Refereeing of this contribution was handled by L. Kaplan.

This work was funded by the Test Resource Management Center (TRMC) Test and Evaluation Science and Technology (T&E/S&T) Program through the U.S. Army Program Executive Office for Simulation, Training and Instrumentation (PEO STRI) under contracts W900KK-09-C-0016 (M4A) and W900KK-13-C-0026 (PAQ).

Authors' addresses: M. Rice, Brigham Young University, Electrical & Computer Engineering, 459 Clyde Building, Provo, UT 84602, E-mail: (mdr@byu.edu); M. S. Afran, M. Saquib, The University of Texas at Dallas, 800 W. Campbell Road, Richardson, Texas 75080-3021.

0018-9251/15/\$26.00 © 2015 IEEE

I. INTRODUCTION

Aeronautical telemetry constitutes a wideband air-to-ground communication link with severe size, weight, and power (SWAP) limitations on the airborne test article. The SWAP issue is addressed by operating the RF power amplifier in full saturation together with a constant envelope modulation. For this reason, the aeronautical telemetry standard Inter Range Instrumentation Group (IRIG) 106 [1] describes three continuous phase modulation (CPM) alternatives for the radio link. As of this writing, shaped offset quadrature phase-shift keying, telemetry group version (SOQPSK-TG) is the most popular of the three. Given the relatively narrow beamwidth of ground-based auto-tracking antennas, the aeronautical telemetry channel is a simple line-of-sight channel when the elevation angle of the airborne test article is sufficiently high. When the elevation angle is lower, multipath interference tends to be the main factor limiting the performance of the link. Given the bandwidth of SOQPSK-TG associated with the bit rates required by modern telemetry systems (10–20 Mb/s) and the delays observed for low-elevation-angle flight paths on test ranges [2–5], multipath fading is almost always frequency selective. The problem is one involving multipath mitigation for a single-carrier, constant-envelope modulation operating in a frequency-selective channel.

The solution involves equalization and/or diversity. Most of the work on equalizing CPM has focused on three major approaches: maximum likelihood sequence estimation based on the composite trellis defined by the signal and the channel [6–9], frequency-domain equalizers [10–19], or blind equalization [8, 20, 21]. In this paper, we focus on linear time-domain equalizers based on the minimum mean-squared error (MMSE) criterion and operating on samples of the SOQPSK-TG signal. This corresponds to time-domain versions of the frequency-domain equalizers described in [10, 18]. The motivation for the time-domain equalizer is the closed form expression for the postequalizer mean-squared error, which is used as the power allocation criterion for the generalized time-reversed space-time block code (GTR-STBC) described in section III. As part of our development, we show that even though the signal samples are cyclostationary, an equalizer designed using an uncorrelated wide-sense stationary assumption provides excellent performance.

The second possible solution is diversity. Diversity reception, especially by widely separated antennas, is an obvious solution that has received a great deal of attention in mobile telephony. However, given the expense of ground-based receiving installations, this solution has been relatively unpopular at the major test range facilities. Transmit diversity, on the other hand, has not been considered as a multipath mitigation technique in aeronautical telemetry. It is well known that the use of multiple transmit antennas is capable of increasing reliability or throughput in multipath fading channels. In

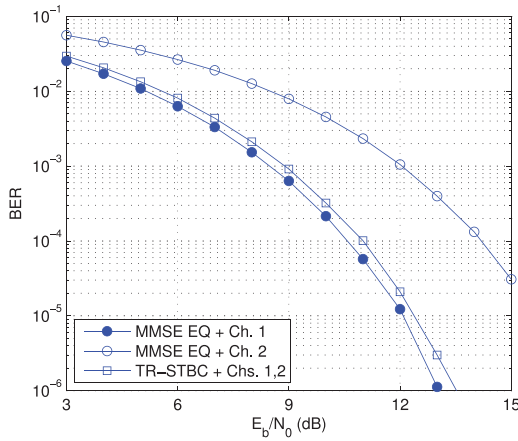


Fig. 1. Simulated BER plots for 10-Mbit/s SOQPSK-TG using MMSE equalizers over a pair of representative impulse responses measured over helicopter-to-ground channel. Circular markers are BER results using single antenna, and square markers are BER results using both channels with TR-STBC.

flat fading, the optimum signaling approach depends on what the transmitter knows [22]. If the transmitter knows the channels between each transmit and receive antenna, then spatio-temporal coding [23] is optimum in that it maximizes signal-to-noise ratio [22]. If the transmitter does not have this knowledge, then a diversity-maximizing approach, such as an orthogonal design like the Alamouti code [24] or space-time trellis codes [25], is optimum [22]. In frequency-selective fading, the general approach is to use OFDM and apply these techniques on a per subcarrier basis. However, given the SWAP constraints, OFDM is not a viable approach in aeronautical telemetry. Consequently, transmit diversity techniques involving single-carrier modulations over frequency-selective channels are of interest. Here, time-reversed space-time block codes (TR-STBCs) [26–30] play the role that the Alamouti code does in frequency-nonselective fading with an uninformed transmitter.

Initial experiments involving TR-STBC with QPSK applied to the helicopter-to-ground channel were reported in [31], where it was observed that TR-STBC does not always provide the best performance when a fixed amount of transmit power must be shared by two transmit antennas. Not surprisingly, the same behavior was also observed when SOQPSK-TG was used. An example is illustrated in Fig. 1. This plot shows simulated bit error rate (BER) performance of SOQPSK-TG using MMSE equalizers (described in section II). The TR-STBC curve (square markers) represents the case where the available transmit power is equally split between the two transmit antennas. The other two curves (circle markers) represent the cases where all of the available power is applied to only one of the two transmit antennas. TR-STBC performs better than the single-channel link using only channel 2 but worse than the single-channel link using only channel 1. Clearly, channel 1 is better, in some sense, than channel 2. In fact, channel 1 is so much better than

channel 2 that incorporating channel 2 into a TR-STBC system only makes things worse.

On flat fading channels, the behavior observed in Fig. 1 is well known and easily explained. For example, if two channels with unequal gains are presented to a transmitter with a fixed amount of available power, the optimum approach is to apply all of the available power to the channel with the highest gain. However, on frequency-selective channels, the situation becomes less clear. Both channel energy (the generalization of channel gain for the frequency-selective case) and the degree of intersymbol interference (ISI) are factors in determining the optimum power allocation. However, the analysis in [31] shows that they are not good predictors of when to apply all available power to one of the antennas or to split the power using TR-STBC.

This paper shows that the postequalizer mean-squared error is a good predictor of this behavior for single-carrier modulations operating over a frequency-selective channel. To show this, we consider a fixed-power transmitter that allocates a portion of the available power to each channel. This power allocation is parameterized by ρ , the proportion of total power allocated to channel 1. Using only one of the two available channels is captured by the case $\rho = 1$ (channel 1 only) or $\rho = 0$ (channel 2 only). Next, we introduce generalized TR-STBC (GTR-STBC), a modified version of TR-STBC that incorporates the unequal power allocation ρ . Because TR-STBC and its generalized version involve the combination of diversity processing and equalization, a suitable equalization technique for SOQPSK-TG is needed. We develop and analyze an MMSE equalizer that operates on the samples of SOQPSK-TG. Equipped with GTR-STBC and the MMSE equalizer, we use the postequalizer mean-squared error to identify the optimum ρ .

In summary, the contributions of this paper are the following:

- 1) We show that a time-domain equalizer operating on the samples of SOQPSK-TG and based on the MMSE criterion using an uncorrelated sample approximation provides excellent performance.
- 2) TR-STBC is generalized to include a power-sharing parameter ρ . We call this generalized TR-STBC or GTR-STBC. Coupling GTR-STBC with MMSE equalizers, we derive the postequalizer mean-squared error as a function of ρ and demonstrate that selecting ρ to minimize the postequalizer mean-squared error defines the power-sharing ratio that minimizes the BER (i.e., it predicts the behavior observed in Fig. 1).
- 3) We apply GTR-STBC to a set of impulse responses measured at two test ranges. The results show that GTR-STBC tends to traditional TR-STBC when the channels are similar (i.e., have similar energies and contribute similar degrees of ISI). When the channels are different, either in energy or contributed ISI, then GTR-STBC tends to transmit selection diversity. These results demonstrate that the optimum power allocation in

measured channels can be quite different from the power allocation suggested using statistical channel models.

4) GTR-STBC was developed as a conceptual tool to explain how a fixed amount of power should be shared between two frequency-selective channels. The conceptual tool can also be used as the basis for a simple transmit diversity scheme where the transmitter need only be equipped with the optimum ρ . The optimum ρ is easily computed by the ground-based receiver and can be uplinked to the transmitter via a low-rate radio link.

This paper is organized as follows. The MMSE equalizer for SOQPSK-TG is developed in section II. GTR-STBC is introduced and analyzed in section III. GTR-STBC is applied to the measured channel impulse responses in section IV, and conclusions are presented in section V.

In the mathematical development, lowercase bold letters (e.g., \mathbf{v}) are used to denote column vectors, and uppercase bold letters (e.g., \mathbf{M}) are used to denote matrices. The transpose operation is denoted \mathbf{v}^T and \mathbf{M}^T ; the Hermitian operation (conjugate-transpose) is denoted \mathbf{v}^\dagger and \mathbf{M}^\dagger ; and for the square matrix \mathbf{M} , \mathbf{M}^{-1} is the matrix inverse.

II. MMSE EQUALIZATION OF SOQPSK-TG

SOQPSK-TG is a partial-response, constrained ternary CPM with modulation index $h = \frac{1}{2}$. The frequency pulse is described in [32, 33]. Because the frequency pulse spans 8 bit times, the maximum likelihood detector in the additive white Gaussian noise (AWGN) environment is a sequence estimator comprising 512 states [32]. The most common detector applied to SOQPSK-TG is the simple OQPSK-type symbol-by-symbol ($S \times S$) detector described in [34]. The $S \times S$ detector consists of a detection filter (see Fig. 3 of [34]), the output of which is sampled at 1 sample/bit and is treated as offset QPSK.

The system considered here is summarized in Fig. 2. The complex-valued baseband equivalent representation [35] is used for all signals. Starting with the block diagram of Fig. 2 (a), the SOQPSK-TG signal $x_c(t)$ is transmitted through a channel with impulse response $h_c(t)$, the output of which, accompanied by thermal noise, forms the receive signal $r_c(t)$. After the application of an anti-aliasing low-pass filter with impulse response $h_a(t)$, T -spaced samples of $r_c(t)$ are produced by an analog-to-digital (A/D) converter. Assuming the anti-aliasing filter does not distort the received signal, the samples of the received signal may be expressed as

$$r(n) = x(n) * h(n) + w(n) = \sum_{k=-L_1}^{L_2} h(k)x(n-k) + w(n), \quad (1)$$

where

$$r(n) = r_c(nT), \quad x(n) = x_c(nT), \\ h(n) = h_c(t) * h_a(t)|_{t=nT},$$

and where $w(n)$ is the n th sample in a sequence of zero-mean complex-valued Gaussian random variables with autocorrelation function

$$R_w(k) = \frac{1}{2} \mathbb{E} \{w(n)w^*(n-k)\} = \sigma_w^2 \delta(k). \quad (2)$$

Note that (1) assumes the discrete-time channel has support on $-L_1 \leq n \leq L_2$. As a first step, we apply the samples $r(n)$ to a filter matched to the discrete-time channel to produce $y(n)$:

$$y(n) = r(n) * h^*(-n) \\ = x(n) * \underbrace{h(n) * h^*(-n)}_{h_{eq}(n)} + \underbrace{w(n) * h^*(-n)}_{v(n)} \quad (3)$$

$$= \sum_{k=-L_{eq}}^{L_{eq}} h_{eq}(k)x(n-k) + v(n), \quad (4)$$

where $L_{eq} = L_1 + L_2$, and $v(n)$ is a complex-valued Gaussian random sequence with zero mean and autocorrelation function

$$R_v(k) = \frac{1}{2} \mathbb{E} \{v(n)v^*(n-k)\} = \sigma_w^2 h_{eq}(k). \quad (5)$$

The samples $y(n)$ form the input to an MMSE equalizer. The MMSE equalizer is a finite impulse response (FIR) filter with coefficients $c(n)$ for $-L_c \leq n \leq L_c$ designed to minimize the mean-squared error between the equalizer filter output $\hat{x}(n)$ and the sequence $x(n)$. The entire system may be represented by an equivalent discrete-time system shown in Fig. 2b.

The challenge with equalizing samples of the modulated signal is that the underlying continuous-time waveform is not wide-sense stationary, but cyclostationary [35]. This fact carries over to the samples of $x_c(t)$ and is captured by the fact that the autocorrelation function of the $x(n)$ is periodic. Consequently, the autocorrelation function is a function of the sample indexes (not the difference between them), so that the optimum equalizer filter coefficients are a function of the sample index n . It is hard to see how this solution has any practical utility, especially in the presence of a real-time performance requirement. In the end, the designer is left with suboptimal approaches of reduced computational complexity for which the accompanying performance penalty is acceptable.

The simplest suboptimal approach is to assume the signal samples are wide-sense stationary. Here, the autocorrelation function is of the form

$$R_x(k-\ell) = \frac{1}{2} \mathbb{E} \{x(k)x^*(\ell)\}, \quad (6)$$

that is, the autocorrelation function depends on the difference of the sample time indexes. The wide-sense stationary assumption for $x(n)$ greatly simplifies the solution. Because the optimum equalizer coefficients no longer depend on the samples index n , the MMSE equalizer reduces to a simple linear time-invariant (LTI) system with impulse response $c(n)$. The equalizer output

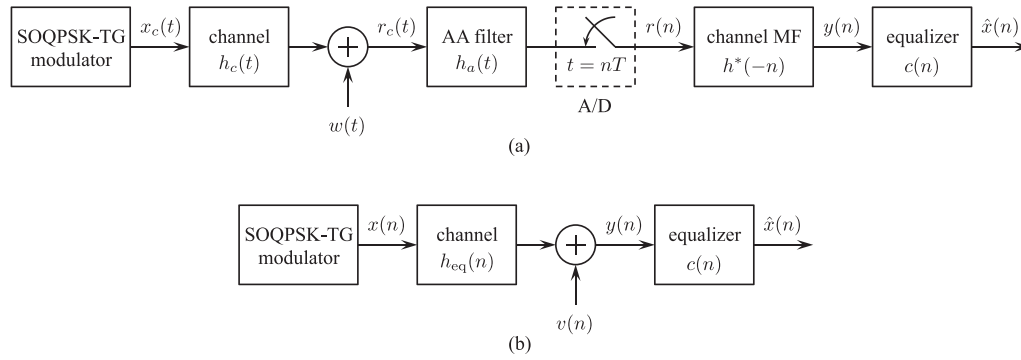


Fig. 2. Block diagram of system that applies MMSE equalizer to samples of received SOQPSK-TG signal: (a) system showing continuous-time signals, anti-aliasing filter, and A/D converter; (b) equivalent discrete-time system.

$\hat{x}(n)$ is thus

$$\hat{x}(n) = c(n) * y(n) = \sum_{k=-L_c}^{L_c} c(k)y(n-k). \quad (7)$$

The vector of filter coefficients that minimizes the mean-squared error

$$\mathcal{E} = E \{|x(n) - \hat{x}(n)|^2\} \quad (8)$$

is given by

$$\mathbf{c} = [\mathbf{G}\mathbf{R}_{x,1}\mathbf{G}^\dagger + \mathbf{R}_v]^{-1}\mathbf{R}_{x,2}\mathbf{g}, \quad (9)$$

where \mathbf{c} is the $(2L_c + 1) \times 1$ vector of filter coefficients, \mathbf{G} is the $(2L_c + 1) \times (2L_c + 1 + 2L_{eq})$ matrix

$\mathbf{R}_{x,2}$ is the $(2L_c + 1) \times (2L_c + 1)$ matrix given by

$$\mathbf{R}_{x,2} = \begin{bmatrix} R_x(0) & R_x(-1) & \cdots & R_x(-2L_c) \\ R_x(1) & R_x(0) & \cdots & R_x(-2L_c + 1) \\ \vdots & \vdots & \ddots & \vdots \\ R_x(2L_c) & R_x(2L_c - 1) & \cdots & R_x(0) \end{bmatrix}; \quad (13)$$

and \mathbf{g} is the $(2L_c + 1) \times 1$ vector given by

$$\mathbf{g} = \begin{bmatrix} \mathbf{0}_{1 \times (L_c - L_{eq})} & \mathbf{h}_{eq}^\dagger & \mathbf{0}_{1 \times (L_c - L_{eq})} \end{bmatrix}^\top, \quad (14)$$

where $\mathbf{0}_{1 \times (L_c - L_{eq})}$ is a row vector comprising $L_c - L_{eq}$ zeros (here we assume $L_c > L_{eq}$, i.e., the equalizer is longer than the channel), and \mathbf{h}_{eq} is the $(2L_{eq} + 1) \times 1$ vector given by

$$\mathbf{h}_{eq} = [h_{eq}(L_{eq}) \cdots h_{eq}(0) \cdots h_{eq}(-L_{eq})]^\top. \quad (15)$$

$$\mathbf{G} = \begin{bmatrix} h_{eq}(L_{eq}) & \cdots & h_{eq}(-L_{eq}) \\ & h_{eq}(L_{eq}) & \cdots & h_{eq}(-L_{eq}) \\ & & \ddots & \\ & & & h_{eq}(L_{eq}) & \cdots & h_{eq}(-L_{eq}) \end{bmatrix}; \quad (10)$$

$\mathbf{R}_{x,1}$ is the $(2L_c + 2L_{eq} + 1) \times (2L_c + 2L_{eq} + 1)$ matrix

$$\mathbf{R}_{x,1} = \begin{bmatrix} R_x(0) & R_x(-1) & \cdots & R_x(-2L_c - 2L_{eq}) \\ R_x(1) & R_x(0) & \cdots & R_x(-2L_c - 2L_{eq} + 1) \\ \vdots & \vdots & \ddots & \vdots \\ R_x(2L_c + 2L_{eq}) & R_x(2L_c + 2L_{eq} - 1) & \cdots & R_x(0) \end{bmatrix}; \quad (11)$$

\mathbf{R}_v is the $(2L_c + 1) \times (2L_c + 1)$ noise autocorrelation matrix given by

$$\mathbf{R}_v = \begin{bmatrix} R_v(0) & \cdots & R_v(-2L_c) \\ \vdots & \ddots & \vdots \\ R_v(2L_c) & \cdots & R_v(0) \end{bmatrix}; \quad (12)$$

We now address the issue of the autocorrelation function $R_x(k)$. Two approximations are investigated here. The first is an empirically derived autocorrelation function. The empirical autocorrelation function is obtained by generating a large number of samples $x(n)$ and using the standard estimation technique assuming wide-sense stationarity. Given L samples of $x(n)$ for $n = 0$,

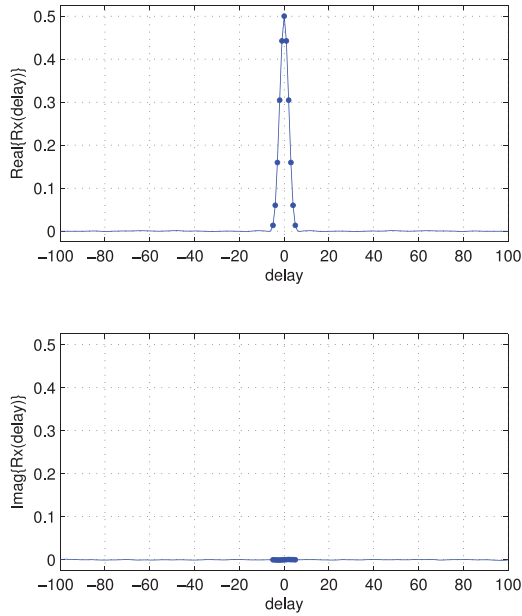


Fig. 3. Plot of empirical autocorrelation function for SOQPSK-TG: (top) real part of $R_e(k)$; (bottom) imaginary part of $R_e(k)$. Sample rate for SOQPSK-TG samples is at 2 samples/bit. Markers indicate values for $-5 \leq k \leq 5$.

$1, \dots, L-1$, this empirical autocorrelation function is

$$R_e(k) = \frac{1}{2(L-k)} \sum_{n=k}^{L-1} x(n)x^*(n-k), \quad 0 \leq k < L-1 \quad (16)$$

together with

$$R_e(k) = R_e^*(-k), \quad -L < k < 0. \quad (17)$$

A plot of $R_e(k)$ corresponding to $L = 2 \times 10^6$ samples of SOQPSK-TG sampled at 2 samples/bit is shown in Fig. 3 for the first 100 lags (i.e., $-100 \leq k \leq 100$). The top plot shows the real part of $R_e(k)$, and the lower plot shows the imaginary part of $R_e(k)$. The only significant values are those for $-5 \leq k \leq 5$, which are indicated by markers on the plot. Consequently, in the simulation results presented below, we assume $R_e(k) = 0$ for $|k| > 5$.

The second approximation is to assume the data are uncorrelated. This generates a correlation function of the form

$$R_i(k) = \sigma_x^2 \delta(k). \quad (18)$$

Here, the corresponding correlation matrices $\mathbf{R}_{x,1}$ and $\mathbf{R}_{x,2}$ reduce to scaled identity matrices.

To test the performance of these approximations, we simulate the performance of the equalized SOQPSK-TG system outlined in Fig. 4. For this test, we use a channel obtained from the channel measurement campaign described below with $L_{eq} = 19$ and operating at $N = 2$ samples/bit. The channel transfer function is plotted in Fig. 5. The equalizer output is applied to the symbol-by-symbol detector for SOQPSK-TG, denoted “S × S detector” in the figure.

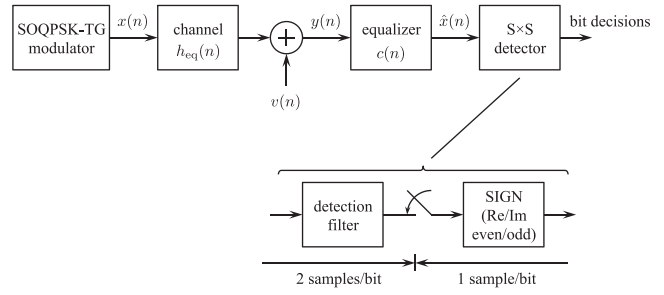


Fig. 4. Block diagram of system used to test performance of SOQPSK-TG autocorrelation assumptions.

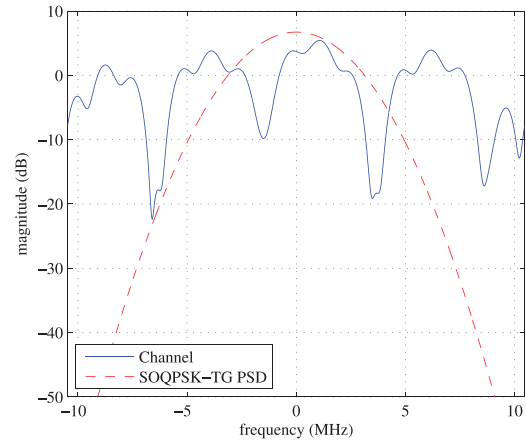


Fig. 5. Channel used in simulations reported in Fig. 6. Channel is obtained from channel measurements described below. Bit rate is 10 Mbits/s, and channel is sampled at 2 samples/bit. Corresponding $h_{eq}(n)$ has $L_{eq} = 19$.

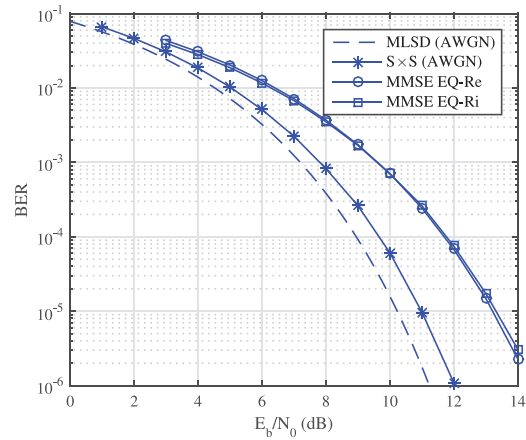


Fig. 6. Simulated BER results for system shown in Fig. 4 using channel illustrated in Fig. 5. Also included for reference is performance of symbol-by-symbol detector in AWGN channel and optimum maximum likelihood sequence detector (MLSD) in AWGN channel (see [34]).

The effectiveness of using $R_e(k)$ and $R_i(k)$ in computing the equalizer coefficients was measured by the simulated BER. The simulations applied the equalizer coefficients obtained from (9) for $L_c = 5 \times L_{eq} = 95$ [36] and using $R_e(k)$ and $R_i(k)$. The simulated BER is plotted in Fig. 6, where we observe that there is essentially no difference in the performance between the two.

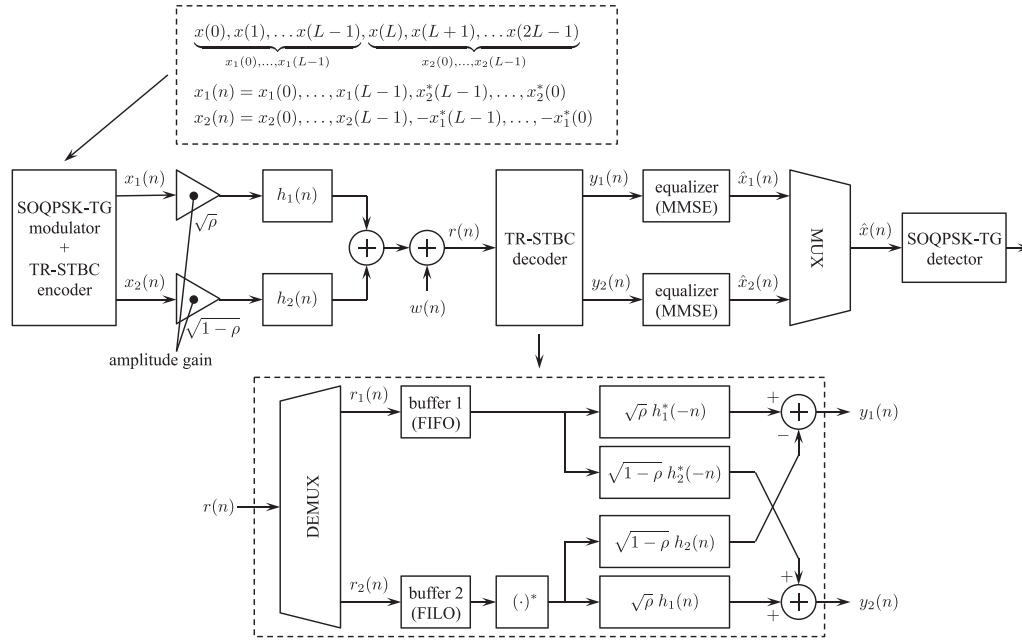


Fig. 7. Block diagram of TR-STBC system based on unequal power allocation using $0 \leq \rho \leq 1$.

Consequently, we prefer $R_i(k)$ over $R_e(k)$ in what follows because this choice simplifies the computations of the equalizer filter coefficients. In this case, the optimum equalizer filter coefficients are given by

$$\mathbf{c} = \left[\mathbf{G}\mathbf{G}^\dagger + \frac{2}{E_b/N_0} \mathbf{H}_{\text{eq}} \right]^{-1} \mathbf{g}, \quad (19)$$

where \mathbf{H}_{eq} is the $(2L_c + 1) \times (2L_c + 1)$ matrix given by

$$\mathbf{H}_{\text{eq}} = \begin{bmatrix} h_{\text{eq}}(0) & \cdots & h_{\text{eq}}(-2L_c) \\ \vdots & & \vdots \\ h_{\text{eq}}(2L_c) & \cdots & h_{\text{eq}}(0) \end{bmatrix}, \quad (20)$$

where it is understood that $h_{\text{eq}}(k) = 0$ for $|k| > L_{\text{eq}}$. The corresponding mean-squared error is

$$\mathcal{E}_{\min} = \sigma_x^2 \left(1 - \mathbf{g}^\dagger \left[\mathbf{G}\mathbf{G}^\dagger + \frac{2}{E_b/N_0} \mathbf{H}_{\text{eq}} \right]^{-1} \mathbf{g} \right). \quad (21)$$

III. GENERALIZED TR-STBC (GTR-STBC)

A. Nonequal Power Allocations Using TR-STBC

An abstraction (to the sample level) for a 2×1 GTR-STBC system is illustrated in Fig. 7. Here, the system transmits $2L$ samples of an SOQPSK-TG signal sampled at N samples/bit over two transmit antennas to one receive antenna. The equivalent discrete-time channel between transmit antenna 1 and the receive antenna is represented by the impulse response $h_1(n)$ for $-L_{1,1} \leq n \leq L_{1,2}$ whereas the equivalent discrete-time channel between transmit antenna 2 and the receive antenna is represented by the impulse response $h_2(n)$ for $-L_{2,1} \leq n \leq L_{2,2}$.

The TR-STBC encoder partitions the sample sequence $x(0), \dots, x(2L-1)$ into two sequences $x_1(n)$ and $x_2(n)$ as shown in Fig. 7. The length- $2L$ packet is transmitted in two intervals,¹ each spanning L sample intervals. During the first interval, $x_1(0), \dots, x_1(L-1)$ is transmitted from antenna 1, whereas $x_2(0), \dots, x_2(L-1)$ is transmitted from antenna 2. During the second interval, $x_2^*(L-1), \dots, x_2^*(0)$ is transmitted from antenna 1, whereas $-x_1^*(L-1), \dots, -x_1^*(0)$ is transmitted from antenna 2.

Power division using $0 \leq \rho \leq 1$ is accomplished by including the two gain blocks shown at the output of the TR-STBC encoder. Amplitude scaling is applied to the signals entering each channel so as to divide the power between the channels. Here, ρ represents the proportion of total power allocated to transmit antenna 1. The traditional TR-STBC system² is a special case for which $\rho = \frac{1}{2}$. The square-root is used in Fig. 7 because the amplitudes are the values being modified—the energy (or power) is the square of the amplitude.

The received signal $r(n)$ is given by

$$r(n) = \sqrt{\rho} x_1(n) * h_1(n) + \sqrt{1-\rho} x_2(n) * h_2(n) + w(n), \quad (22)$$

where $w(n)$ is a complex-valued Gaussian random sequence with zero mean and autocovariance function

¹ In a practical implementation, a guard interval at least as long as the longest channel impulse response must be inserted between the two intervals. Here, such an interval is assumed, although we do not complicate the notation to make this explicit.

² In the traditional TR-STBC system, $\rho = \frac{1}{2}$ is included in neither the development nor the notation because the same power is assumed to be applied to each channel. Hence, there is no need to account for it, other than in normalizing the noise variance.

given by (2). The GTR-STBC decoder partitions $r(n)$ into $r_1(n)$ and $r_2(n)$ as follows:

$$\begin{aligned} r_1(n) &= r(n) \text{ for } 0 \leq n \leq L-1 \\ r_2(n-L) &= r(n) \text{ for } L \leq n \leq 2L-1. \end{aligned} \quad (23)$$

These two sequences are given by

$$\begin{aligned} r_1(n) &= \sqrt{\rho} x_1(n) * h_1(n) + \sqrt{1-\rho} \\ &\quad \times x_2(n) * h_2(n) + w_1(n) \end{aligned} \quad (24)$$

and

$$\begin{aligned} r_2(n) &= \sqrt{\rho} x_2^*(-n) * h_1(n) - \sqrt{1-\rho} \\ &\quad \times x_1^*(-n) * h_2(n) + w_2(n), \end{aligned} \quad (25)$$

where $w_1(n)$ and $w_2(n)$ are related to $w(n)$ in the same way as $r_1(n)$ and $r_2(n)$ are related to $r(n)$. The GTR-STBC decoder processes $r_1(n)$ and $r_2(n)$ using a bank of filters based on the channel impulse responses $h_1(n)$ and $h_2(n)$ as shown. The result of this processing is a pair of parallel sequences $y_1(n)$ and $y_2(n)$, which may be expressed as

$$\begin{aligned} y_1(n) &= r_1(n) * \sqrt{\rho} h_1^*(-n) - r_2^*(-n) * \sqrt{1-\rho} h_2(n) \\ &= x_1(n) * \underbrace{[\rho h_1(n) * h_1^*(-n) + (1-\rho) h_2(n) * h_2^*(-n)]}_{h_{\text{eq}}(n)} \\ &\quad + \underbrace{[w_1(n) * \sqrt{\rho} h_1^*(-n) + w_2^*(-n) * \sqrt{1-\rho} h_2(n)]}_{v_1(n)} \end{aligned} \quad (26)$$

and

$$\begin{aligned} y_2(n) &= r_1(n) * \sqrt{1-\rho} h_2^*(-n) + r_2^*(-n) * \sqrt{\rho} h_1(n) \\ &= x_2(n) * \underbrace{[(1-\rho) h_2(n) * h_2^*(-n) + \rho h_1^*(-n) * h_1(n)]}_{h_{\text{eq}}(n)} \\ &\quad + \underbrace{[\sqrt{1-\rho} w_1(n) * h_2^*(-n) + \sqrt{\rho} w_2^*(-n) * h_1(n)]}_{v_2(n)}. \end{aligned} \quad (27)$$

These equations show that the equivalent composite channel for nonequal power allocation is

$$h_{\text{eq}}(n) = \rho \underbrace{h_1(n) * h_1^*(-n)}_{\eta_1(n)} + (1-\rho) \underbrace{h_2(n) * h_2^*(-n)}_{\eta_2(n)}. \quad (28)$$

Because the support for $h_1(n)$ is $-L_{1,1} \leq n \leq L_{1,2}$, the support for $\eta_1(n)$ is $-(L_{1,1} + L_{1,2}) \leq n \leq (L_{1,1} + L_{1,2})$. Similarly, because the support for $h_2(n)$ is $-L_{2,1} \leq n \leq L_{2,2}$, the support for $\eta_2(n)$ is $-(L_{2,1} + L_{2,2}) \leq n \leq (L_{2,1} + L_{2,2})$. Consequently, the support for $h_{\text{eq}}(n)$ is $-L_{\text{eq}} \leq n \leq L_{\text{eq}}$, where

$$L_{\text{eq}} = \max \{L_{1,1} + L_{1,2}, L_{2,1} + L_{2,2}\}. \quad (29)$$

The noise sequences $v_1(n)$ and $v_2(n)$ are complex-valued Gaussian random sequences, each with zero mean and autocorrelation and cross-correlation

functions

$$\frac{1}{2} \mathbb{E} \{v_1(n) v_1^*(n-k)\} = \frac{1}{2} \mathbb{E} \{v_2(n) v_2^*(n-k)\} = \sigma_w^2 h_{\text{eq}}(k). \quad (30)$$

$$\mathbb{E} \{v_1(n) v_2^*(n-k)\} = 0. \quad (31)$$

By way of summary, the GTR-STBC system presents to the equalizers the sequences $y_1(n)$ and $y_2(n)$, which may be represented by

$$y_1(n) = x_1(n) * h_{\text{eq}}(n) + v_1(n) \quad (32)$$

and

$$y_2(n) = x_2(n) * h_{\text{eq}}(n) + v_2(n), \quad (33)$$

where $h_{\text{eq}}(n)$ is given by (28). The noise terms $v_1(n)$ and $v_2(n)$ are uncorrelated zero-mean Gaussian random sequences, each with autocorrelation function (30). A pair of equalizers operate in parallel on $y_1(n)$ and $y_2(n)$. Because the noise sequences $v_1(n)$ and $v_2(n)$ are statistically equivalent, and $h_{\text{eq}}(n)$ is common to both, the pair of equalizers operating on $y_1(n)$ and $y_2(n)$ are identical as long as $x_1(n)$ and $x_2(n)$ are statistically equivalent (the usual case). Any equalizer can be applied here (linear or nonlinear, with or without noise whitening) with the usual performance-complexity trade-offs. For the approximate MMSE equalizer described in section II, the vector of filter coefficients is given by (19), and the corresponding mean-squared error is given by (21). In these equations, \mathbf{G} , \mathbf{g} , and \mathbf{H}_{eq} may be expressed in terms of power allocation parameter ρ . Using (28), it is straightforward to show that

$$\mathbf{G} = \rho \mathbf{G}_1 + (1-\rho) \mathbf{G}_2, \quad (34)$$

$$\mathbf{g} = \rho \mathbf{g}_1 + (1-\rho) \mathbf{g}_2, \quad (35)$$

$$\mathbf{H}_{\text{eq}} = \rho \mathbf{H}_1 + (1-\rho) \mathbf{H}_2, \quad (36)$$

where \mathbf{G}_1 , \mathbf{g}_1 , and \mathbf{H}_1 are formed from $\eta_1(n)$ in the same way as \mathbf{G} , \mathbf{g} , and \mathbf{H}_{eq} are formed from $h_{\text{eq}}(n)$, respectively. Similar definitions apply to \mathbf{G}_2 , \mathbf{g}_2 , and \mathbf{H}_2 with $\eta_2(n)$.

Making the substitutions for \mathbf{G} , \mathbf{g} , and \mathbf{H}_{eq} gives

$$\mathbf{c} = \mathbf{M}(\rho)^{-1} (\rho \mathbf{g}_1 + (1-\rho) \mathbf{g}_2) \quad (37)$$

and

$$\begin{aligned} \mathcal{E}_{\min} &= \sigma_x^2 [1 - (\rho \mathbf{g}_1 + (1-\rho) \mathbf{g}_2)^\dagger \mathbf{M}(\rho)^{-1} \\ &\quad \times (\rho \mathbf{g}_1 + (1-\rho) \mathbf{g}_2)], \end{aligned} \quad (38)$$

where

$$\begin{aligned} \mathbf{M}(\rho) &= (\rho \mathbf{G}_1 + (1-\rho) \mathbf{G}_2) (\rho \mathbf{G}_1 + (1-\rho) \mathbf{G}_2)^\dagger \\ &\quad + \frac{2}{E_b/N_0} (\rho \mathbf{H}_1 + (1-\rho) \mathbf{H}_2). \end{aligned} \quad (39)$$

We adopt the postequalizer mean-squared error as the criterion for identifying the optimum power-sharing parameter ρ . The motivations for the mean-squared error criterion are the following:

- 1) A mathematically tractable expression for the postequalizer mean-squared error is available; see (38).
- 2) The mean-square error criterion neatly captures the contributions of both ISI and additive noise at the equalizer output.
- 3) Generally speaking, reductions in mean-squared error lead to reductions in BER.

The simulation results presented next demonstrate this to be true in our application. By expressing the postequalizer mean-squared error as a function of ρ , the value of ρ that minimizes the postequalizer mean-squared error can be easily identified. Thus, for a given pair of channels $h_1(n)$ and $h_2(n)$, one can choose the power allocation to minimize the postequalizer mean-squared error.

IV. NUMERICAL RESULTS

The forgoing analysis was applied to measured impulse responses from four multipath environments typically encountered in aeronautical telemetry. In the numerical results presented in the next three sections, impulse responses derived from the channel sounding experiments described in [4, 5] were used. Let $h_{1,u}(n)$ and $h_{2,u}(n)$ be unnormalized impulse responses for the two equivalent discrete-time channels obtained directly from the channel sounding data. In a two-transmit, one-receive antenna system operating in a flat fading environment, the two channels rarely have the same gain. The same is true in the case of two frequency-selective fading channels if we replace “gain” with the energy in the two impulse responses:

$$E_1 = \sum_{n=-L_{1,1}}^{L_{1,2}} |h_{1,u}(n)|^2, \quad E_2 = \sum_{n=-L_{2,1}}^{L_{2,2}} |h_{2,u}(n)|^2. \quad (40)$$

Note that E_i reduces to the flat fading (power) gain when $L_{i,1} = L_{i,2} = 0$ for $i = 1, 2$.

In the numerical results, the natural normalization simply scales the stronger of the two channels to have unit energy:

$$h_1(n) = \frac{1}{\sqrt{E}} h_{1,u}(n), \quad h_2(n) = \frac{1}{\sqrt{E}} h_{2,u}(n) \quad (41)$$

where $E = \max\{E_1, E_2\}$. The motivation is simple: scaling the noise to achieve a desired signal-to-noise ratio is more convenient.

A second normalization is also examined in the numerical results. This normalization, called the equal-energy normalization, scales both channels to have unit energy:

$$h_1(n) = \frac{1}{\sqrt{E_1}} h_{1,u}(n), \quad h_2(n) = \frac{1}{\sqrt{E_2}} h_{2,u}(n). \quad (42)$$

The equal-energy normalization is typical of statistical or mathematical models of multi-antenna propagation and is a common feature of the more academic approach, see, e.g., [37].

The normalization impacts the postequalization mean-squared error and consequently the optimum value of ρ . The relationship between the normalization and the optimum ρ is complicated. The MMSE equalizer finds the best balance between residual ISI and noise enhancement for the composite channel $h_{eq}(n)$. As ρ varies, the contributions by the constituent channels $h_1(n)$ and $h_2(n)$ to $h_{eq}(n)$ change the degree of ISI and the energy of the channel relative to the additive noise. The natural normalization preserves the differences between “strong” and “weak” channels (as defined by their energies). In contrast, the equal-energy normalization tends to de-emphasize the differences between “strong” and “weak” channels and emphasize differences in ISI. This explains the observed impact of normalization on the optimum value of ρ in the numerical results.

The numerical results were produced as follows. We assume 10 Mbit/s SOQPSK-TG with the equalizers operating at 2 samples/bit. In each of the four cases, we compute the optimum power allocation parameter ρ to a pair of channels labeled $h_1(n)$ and $h_2(n)$. The physical meaning of these channels depends on the scenario as described below. For each pair of channel impulse responses, the impulse responses were normalized using one of the two procedures described above. The value of ρ that minimizes³ (38) the result for $L_c = 5 \times L_{eq}$ [36] was computed.

A. Cairns Army Airfield, Ft. Rucker, Alabama

The first data set consists of channel impulse responses collected at Cairns Army Airfield, Ft. Rucker, Alabama. Here, the transmitter was a UH-1H helicopter equipped with 4 transmit antennas as illustrated in Fig. 8. The helicopter flight path, the multipath environment, and the locations of the receive antennas are shown in Fig. 9. The ground station was composed of 1.8-m-diameter and 1.2-m-diameter tracking dishes, labeled RX1 and RX2, respectively, located as shown in Fig. 8. The channel sounding signal, occupying 50 MHz of bandwidth and centered at 1800 MHz (upper L-band), was used to probe the channel. The resulting impulse responses were resampled to 20 Msamples/s to produce a channel for 10 Mbit/s SOQPSK-TG sampled at 2 samples/bit. Additional details are available in [4].

During the flight-line run, the UH-1H maintained an altitude between 4.6 and 6.1 m above ground level (AGL). The receive antennas were positioned on 18.3 m towers. The hangers along the flight line are also 18.3 m tall at the roof centers. Consequently, line-of-sight propagation was not possible when a hanger was between the UH-1H and the receive antennas.

To illustrate the behavior of ρ , we assign the resampled version of $h_{c,2,1}(t)$ (transmission from the nose antenna) to $h_1(n)$ and the resampled version of $h_{c,2,4}(t)$ (transmission from the tail antenna) to $h_2(n)$. The

³ The minimization was carried out using a golden section search over the interval $0 \leq \rho \leq 1$ and parabolic interpolation (MATLAB[®]'s `fminbnd`).

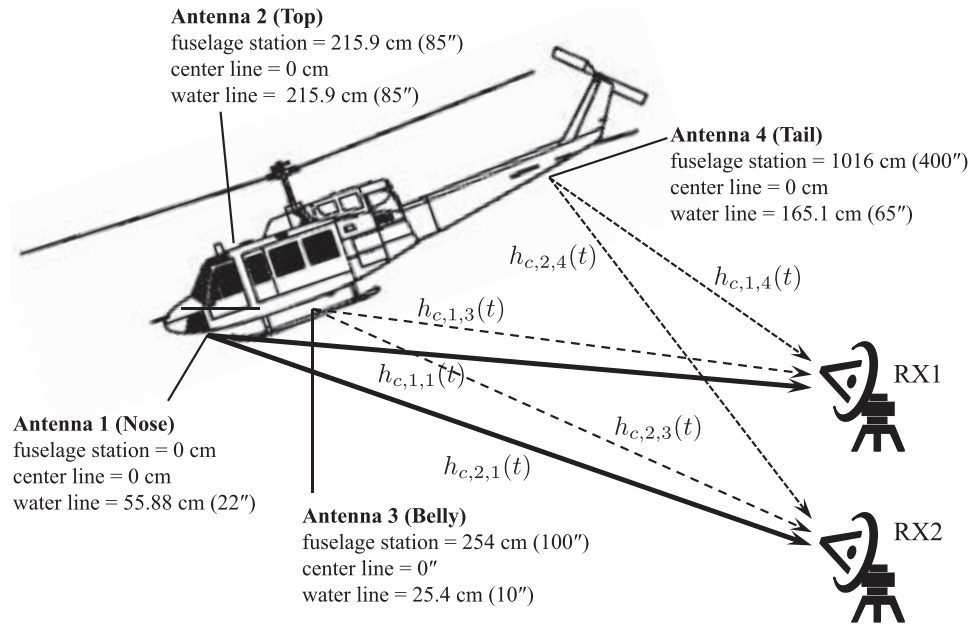


Fig. 8. Diagram of helicopter-to-ground multi-antenna communications link. Here, $h_{c,ji}(t)$ is continuous-time impulse response of channel between transmit antenna i and receive antenna j for $i \in \{1,3,4\}$ and $j \in \{1,2\}$.



Fig. 9. Flight path for UH-1H helicopter and locations of two receive antennas for multipath channel sounding experiments at Cairns Army Airfield, Ft. Rucker, Alabama. Two receive antennas are located on towers at bottom of figure.

forward-to-aft separation between the two transmit antennas is 1016 cm (approximately 61 wavelengths at 1800 MHz). When the UH-1H is level, tail antenna is 109.22 cm (approximately $6\frac{1}{2}$ wavelengths at 1800 MHz) higher than the nose antenna. During flight, the helicopter pitches forward (as suggested in Fig. 8), and this places the tail antenna somewhat more than 109.22 cm higher than the nose antenna.

The locations of the two transmit antennas and the receive antenna produce impulse responses with significant (and similar) degrees of ISI and similar energies, although there were locations where the

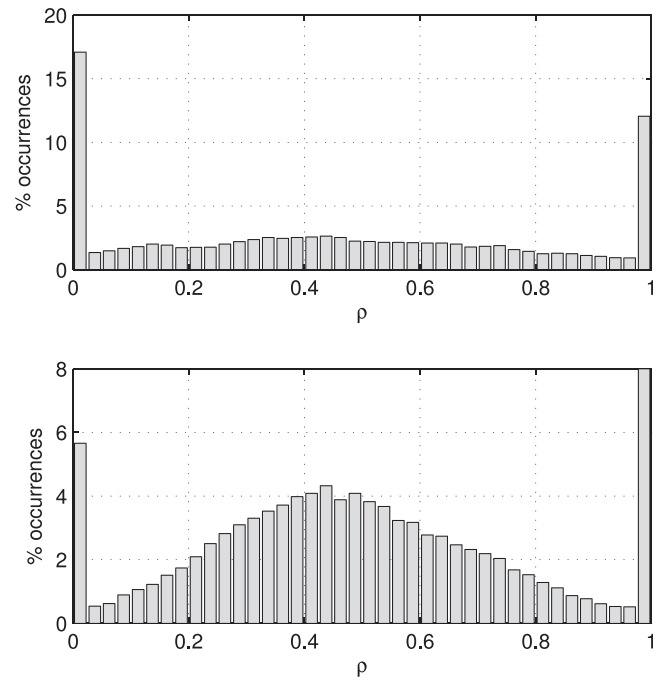


Fig. 10. Optimum power allocations for measured channel impulse responses from Cairns Army Airfield, Ft. Rucker, Alabama, using natural normalization: (top) $E_b/N_0 = 10$ dB; (bottom) $E_b/N_0 = 20$ dB.

propagation path between one of the two transmit antennas and the receiver was more attenuated than the other, and where the ISI on one channel was much less severe than on the other. Thus, this set of 39300 impulse response pairs represents a rich mixture of varying signal-to-noise ratios and ISI.

The results using the natural normalization are summarized by the histograms shown in Fig. 10.

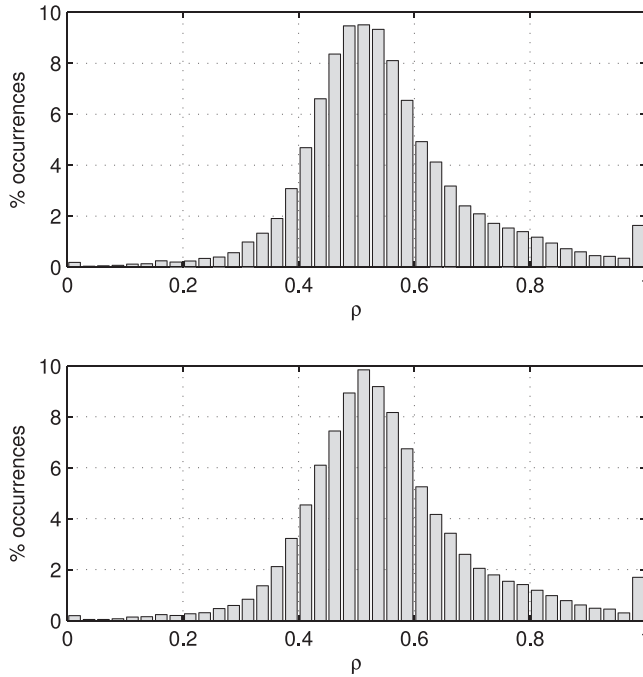


Fig. 11. Optimum power allocations for measured channel impulse responses from Cairns Army Airfield, Ft. Rucker, Alabama, using equal-energy normalization: (top) $E_b/N_0 = 10$ dB; (bottom) $E_b/N_0 = 20$ dB.

Curiously, 11454 of the 39300 values of ρ for $E_b/N_0 = 10$ dB (the top histogram in Fig. 10) are close to either 0 or 1. This means approximately 29% of the channel pairs prefer the use of a single channel over the use of both channels. The remaining 27846 channel pairs minimize the mean-squared error by applying some portion of the available transmit power to both antennas. As the signal-to-noise ratio increases to 20 dB (the bottom histogram Fig. 10), the number of occurrences where the single-antenna solution is best falls to 5366, or 14% of the channel pairs. This indicates that as signal-to-noise ratio increases, ISI plays an increasingly dominant role in determining the power allocation that minimizes the mean-squared error. The more similar a pair of channels are from the ISI point of view, the more $\rho = \frac{1}{2}$ minimizes the mean-squared error. This suggests that when the signal-to-noise ratio penalty is removed from the weaker of the two channels, an even stronger preference for $\rho = \frac{1}{2}$ should be observed.

That this is true is documented by the histograms in Fig. 11. In the top histogram of Fig. 11, 710 of the 39300 channel pairs (2%) prefer only one of the channels when $E_b/N_0 = 10$ dB, while in the bottom histogram of Fig. 11, 743 of the 39300 channel pairs (2%) prefer only one of the channels when $E_b/N_0 = 20$ dB.

Insight into the potential BER improvement offered by GTR-STBC with the natural normalization is shown in Fig. 12. These simulated BER curves were generated as follows. We randomly selected 1000 channel impulse responses from the 39300 channel impulses responses in this data set. For each impulse response, the equalized

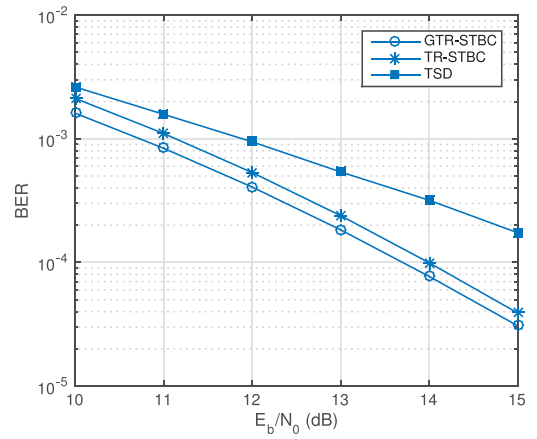


Fig. 12. Comparison of average simulated BER for 1000 randomly selected channels from 39300 channel impulse responses measured at Cairns Army Airfield, Ft. Rucker, Alabama (cf. Fig. 10).

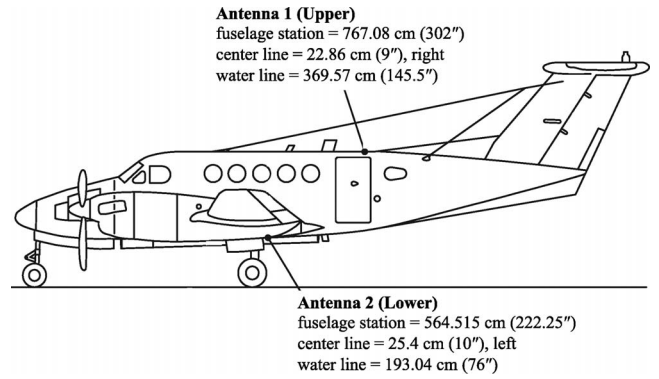


Fig. 13. Diagram of airborne platform for channel sounding experiments at Edwards Air Force Base, California, showing locations of transmit antennas.

BER performance was simulated using GTR-STBC, traditional TR-STBC (i.e., GTR-STBC with fixed $\rho = \frac{1}{2}$), and “transmit selection diversity” or TSD (i.e., GTR-STBC with $\rho \in \{0, 1\}$), whichever produced the lowest simulated BER). For each value of E_b/N_0 , the 1000 simulated BER results for GTR-STBC were averaged to produce the GTR-STBC curve shown in the figure. Identical averaging was performed with the TR-STBC and TSD simulation results.

The curves show that, on average, GTR-STBC is better than the other two at the values of E_b/N_0 shown. This is to be expected: Because traditional TR-STBC and TSD are special cases of GTR-STBC, GTR-STBC will be equal to or better than the other two for any given channel pair and for any E_b/N_0 . At $E_b/N_0 = 10$ dB, all three STBCs achieve nearly the same BER performance. The data in the top plot of Fig. 10 predict this: GTR-STBC and TSD are equivalent for 29% of the channel impulse responses, so one expects the GTR-STBC and TSD performance to be similar. Interestingly, the TR-STBC performance is also much the same. As E_b/N_0 increases, both GTR-STBC and traditional TR-STBC show an increasing performance gain relative to TSD. The data in the bottom plot of

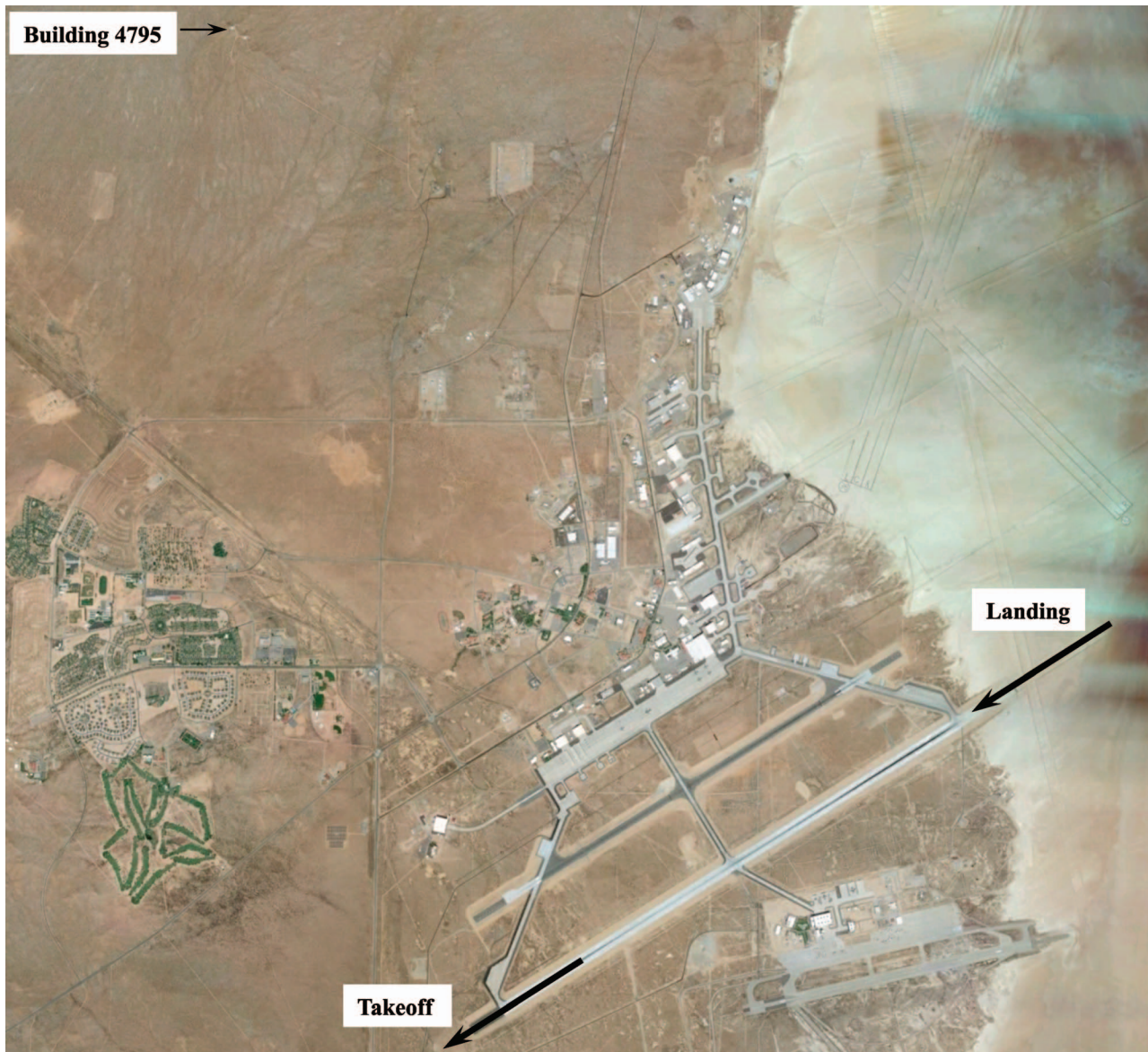


Fig. 14. Map of Edwards Air Force Base, California, showing location of ground (receiving) station at Building 4795 (upper-left corner of map) and locations of aircraft during takeoff and landing (bottom-right corner of the map).

Fig. 10 predict this: At $E_b/N_0 = 20$ dB, TSD is optimum for only 14% of the channel impulse responses. This means power allocation to both channels is the best approach. The difference in BER between the TSD curve and the GTR-STBC and TR-STBC curves shows that the difference in BER performance is noteworthy. For this particular data set, the performance improvement offered by GTR-STBC over TR-STBC is not large (less than 1 dB at 10^{-4} BER). This is because on average, the two channels have similar energies. In cases where the channels have different energies, the performance of TSD will be close to that of GTR-STBC, and the difference in BER performance between GTR-STBC/TSD and TR-STBC will be noteworthy.

In summary, the results for a multipath-rich environment show that when signal-to-noise ratio is moderate, and the channels are not normalized to equal

energy, applying 100% of the available power to one of the two transmit antennas is frequently the solution that minimizes the mean-squared error. As signal-to-noise ratio increases, or the signal-to-noise ratio penalty of the weaker channel is removed, applying 100% of the available power to one of the two antennas is less often the solution that minimizes the mean-squared error. In this case, as long as the channels have similar degrees of ISI, applying power to both channels becomes the best thing to do.

B. Edwards Air Force Base, California—Takeoff and Landing

This data set consists of channel impulse responses collected at Edwards Air Force Base, California. Here, the transmitter was a Beechcraft C-12 equipped with two transmit antennas as illustrated in Fig. 13. The antennas are separated by 201.295 cm (approximately 12

wavelengths at 1824.5 MHz) in the forward/aft direction and 176.53 cm (approximately 11 wavelengths at 1824.5 MHz) in the up/down direction. The ground station, equipped with an 5 m parabolic reflector autotracking antenna, was located at Building 4795 (34°58'14.52"N, 117°55'52.68"W) as shown in Fig. 14. The channel sounding signal, occupying 50 MHz of bandwidth and centered at 1824.5 MHz (upper L-band), was used to probe the channel. The resulting impulse responses were resampled to 20 Msamples/s to produce a discrete-time channel for 10 Mbit/s SOQPSK-TG sampled at 2 samples/bit. See [5] for more details.

The focus of this section is the takeoff and landing test points on runway 22 L as shown in Fig. 14. Building 5790 is approximately 8.75 km from each end of runway 22 L and 120 m higher in elevation. This permits at least a partially unobstructed view of the aircraft when it is on either end of the runway. The multipath environment consists of ground reflections and reflections from structures in the line-of-sight path between the aircraft and the ground-station tracking antenna. Given the narrow beamwidth of the tracking antenna (approximately 2.3° null-to-null), multipath interference tends to disappear once the aircraft achieves a modest altitude (approximately 175 m above the runway).

To illustrate the behavior of ρ for takeoff and landing, $h_1(n)$ is assigned to the resampled version of the upper-antenna-to-ground propagation path, and $h_2(n)$ is assigned to the resampled version of the lower-antenna-to-ground propagation path. The geometry is such that the propagation path between the lower antenna and the receiver is partially obscured by the aircraft fuselage. Consequently, $h_1(n)$ is accompanied by a higher signal-to-noise ratio than $h_2(n)$. The lower antenna is further penalized by the presence of a more direct path to the ground-based reflectors that produce multipath. Thus, $h_2(n)$ has more ISI than $h_1(n)$. This double penalty of lower signal-to-noise ratio and higher ISI should skew the optimum power allocation in favor of $h_1(n)$ (that is, $\rho \approx 1$).

The results, summarized in Figs. 15 and 16 for the 12564 pairs of channel impulse responses, show that this prediction is mostly true. As expected, applying 100% of the available power to the upper antenna dominates the solutions that minimize the mean-squared error for both normalization modes: 11800 or 94% for $E_b/N_0 = 10$ dB and 11894 or 95% for $E_b/N_0 = 20$ dB with the natural normalization; 11850 or 94% for $E_b/N_0 = 10$ dB and 11894 or 95% for $E_b/N_0 = 20$ dB with the equal-energy normalization. The few alternatives to this solution are those where 100% of the available power is allocated to the lower antenna. This is probably explained by the fact that because the two antennas are separated by several wavelengths, the two multipath channels are well approximated as independent channels: When $h_1(n)$ is experiencing significant ISI, $h_2(n)$ can be relatively ISI-free. Furthermore, when the energy of $h_2(n)$ is significantly below that of $h_1(n)$, the contribution of the

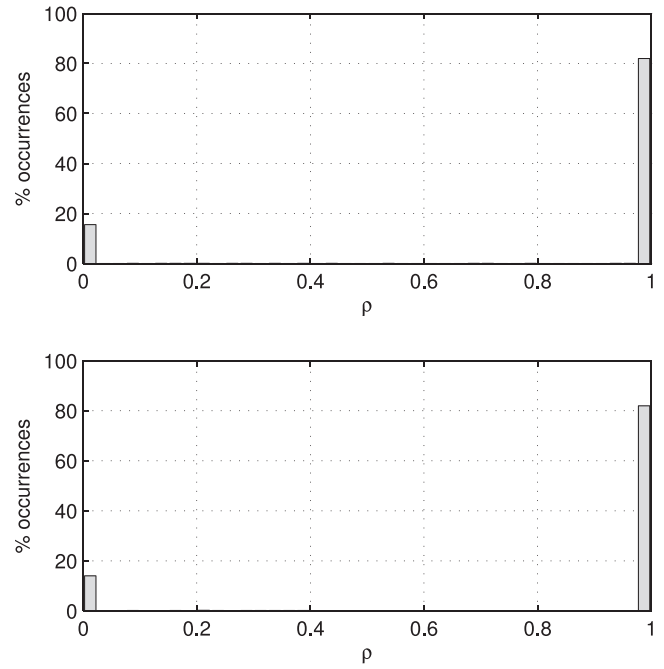


Fig. 15. Optimum power allocations for measured channel impulse responses from takeoff and landing on runway 22 L at Edwards Air Force Base, California, using natural normalization: (top) $E_b/N_0 = 10$ dB; (bottom) $E_b/N_0 = 20$ dB.

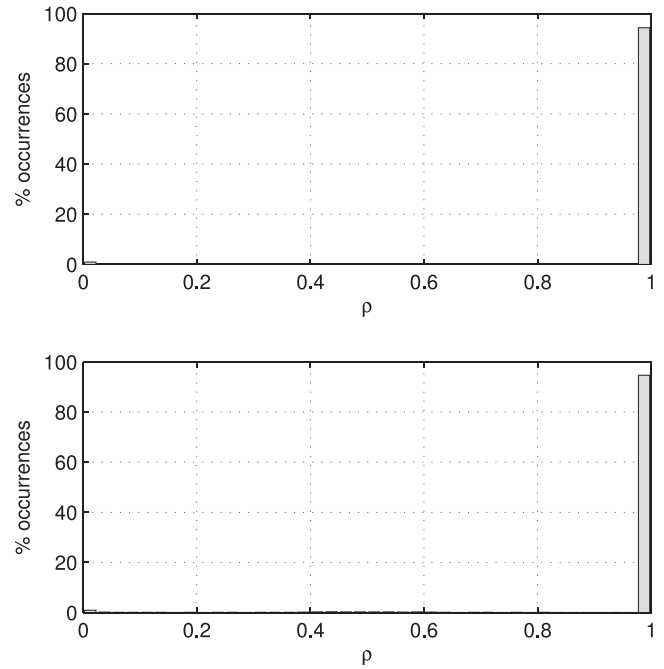


Fig. 16. Optimum power allocations for measured channel impulse responses from takeoff and landing on runway 22 L at Edwards Air Force Base, California, using equal-energy normalization: (top) $E_b/N_0 = 10$ dB; (bottom) $E_b/N_0 = 20$ dB.

ISI associated with $h_2(n)$ to the overall mean-squared error is less. The figures show that as signal-to-noise ratio increases, the scenarios where $\rho = 0$ minimizes mean-squared error become less frequent.

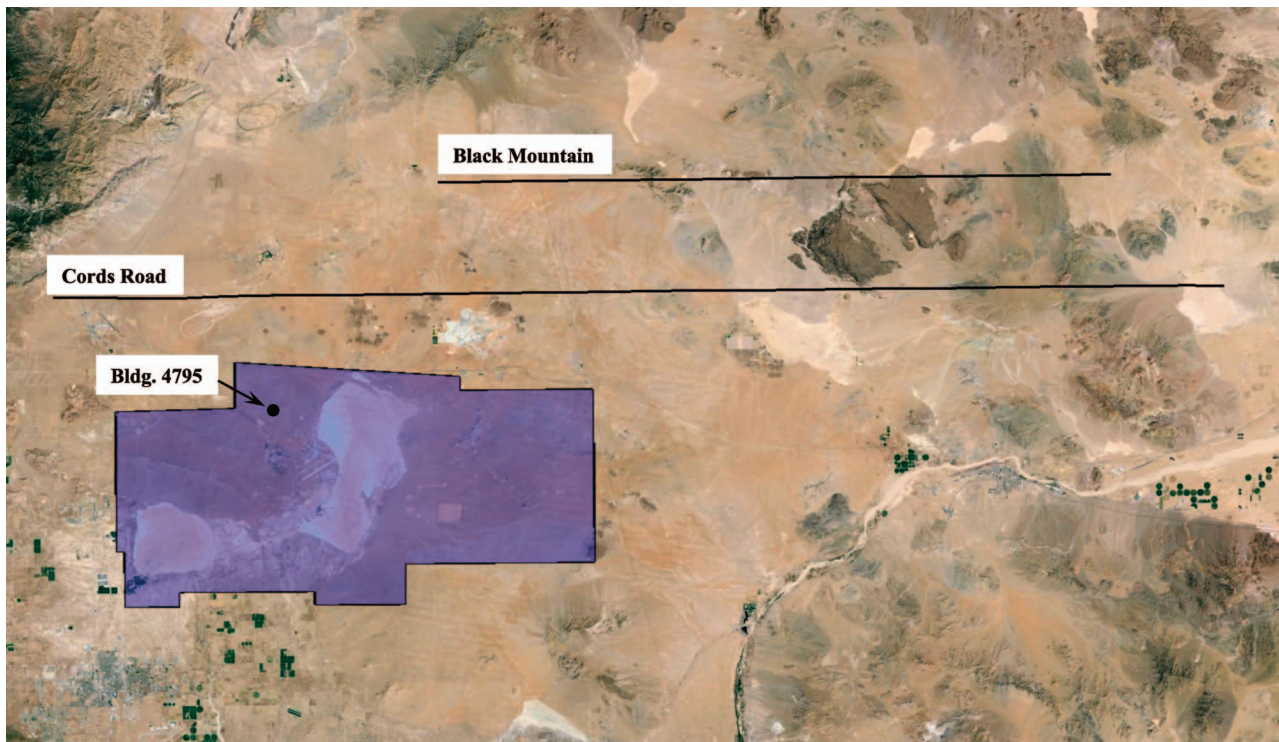


Fig. 17. Map of Edwards Air Force Base, California, showing location of ground (receiving) station at Building 4795 and flight paths for Black Mountain and Cords Road flight paths.

In summary, the takeoff and landing scenario at Edwards Air Force Base, California, is characterized by a geometric arrangement where one of the two channels is inferior in both signal-to-noise ratio and ISI. The solution that minimizes the mean-squared error is the one where all the available power is applied to the good antenna, and the percentage of the cases where this is the solution increases with signal-to-noise ratio.

C. Edwards Air Force Base, California—Black Mountain and Cords Road

These two data sets consist of channel impulse responses also collected at Edwards Air Force, California. The airborne transmitter, ground station, and center frequency described in section IVB were used to obtain these data sets. What is different is the flight path. The two flight paths, called Black Mountain and Cords Road, together with their geographic relationship to the ground station (Building 4795) are shown in Fig. 17. The Black Mountain flight path is an east-west flight corridor from $35^{\circ}12'00''\text{N}$, $116^{\circ}50'00''\text{W}$ to $35^{\circ}12'00''\text{N}$, $117^{\circ}56'00''\text{W}$. The Cords Road flight path is also an east-west flight corridor south of the Black Mountain flight path and extends from $35^{\circ}05'00''\text{N}$, $116^{\circ}42'00''\text{W}$ to $35^{\circ}05'00''\text{N}$, $118^{\circ}22'00''\text{W}$. For both flight paths, the airborne transmitter maintained an altitude of 1524 m above mean sea level (AMSL). These flight paths are important in that they capture the behavior of low-elevation-angle “up-and-away” flight paths. An important characteristic of

this flight geometry is the low elevation angle of the receive antenna. The elevation angle is low due to the large distances between the airborne transmitter and the ground-based receiver. (Building 4795 is approximately 32 km and 100 km from the west and east ends of the Black Mountain flight path, respectively, and 29 km and 111 km from the west and east ends of the Cords Road flight path, respectively.) Because of the low elevation angles, air-to-ground propagation is prone to multipath interference from strong “ground bounces” [2].

As in section IVB, $h_1(n)$ represents the resampled version of the upper-antenna-to-ground propagation path, whereas $h_2(n)$ represents the resampled version of the lower-antenna-to-ground propagation path. Because of the geometry, the upper antenna is partially masked by the aircraft fuselage. Consequently, the signal received from the lower antenna is stronger. Thus, $h_2(n)$ is characterized by a higher signal-to-noise ratio than $h_1(n)$. However, the lower antenna also illuminates the ground (the source of most of the multipath reflections) with a stronger signal than the upper antenna. Thus, although $h_2(n)$ has a higher signal-to-noise ratio than $h_1(n)$, $h_2(n)$ also has more ISI than $h_1(n)$. In this way, the Black Mountain and Cords Road flight paths present a scenario involving a signal-to-noise ratio and ISI trade-off. How this trade-off interacts with ρ to minimize the achievable mean-squared error is the open question here.

The results for the 190716 pairs of channel impulse responses for the Black Mountain flight path are summarized by the histograms in Figs. 18 and 19. The

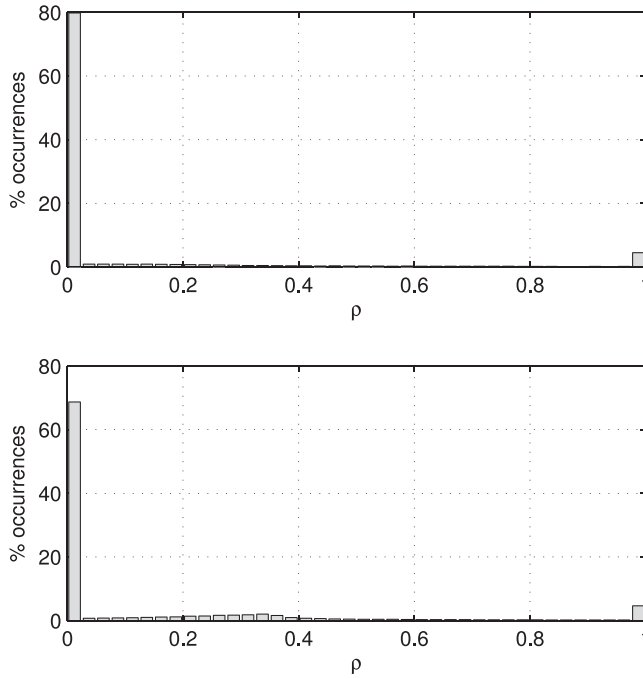


Fig. 18. Optimum power allocations for measured channel impulse responses from Black Mountain flight path at Edwards Air Force Base, California, using natural normalization: (top) $E_b/N_0 = 10$ dB; (bottom) $E_b/N_0 = 20$ dB.

results corresponding to the natural normalization are shown in Fig. 18. Here, the ISI is such that the equalizer is able to reduce the residual ISI to the point where signal-to-noise ratio is the dominant factor. The end result is that the ISI, signal-to-noise ratio, and power allocation trade-off become mostly a trade-off between signal-to-noise ratio and power allocation. This trade-off is such that the mean-squared error is minimized by applying 100% of the available power to the lower antenna [corresponding to $h_2(n)$] in the vast majority of the cases (152246 or 80% for $E_b/N_0 = 10$ dB, 130989 or 69% for $E_b/N_0 = 20$ dB). With the equal-energy normalization, the signal-to-noise ratio penalty associated with $h_1(n)$ is removed, and the trade-off reduces to an ISI versus signal-to-noise ratio trade-off. In this case, summarized in Fig. 19, the situation reverses. The mean-squared error is minimized by applying 100% of the available power to the upper antenna in the vast majority of the cases (147738 or 77% for $E_b/N_0 = 10$ dB, and 155786 or 82% for $E_b/N_0 = 20$ dB).

The results for the 154305 pairs of channel impulse responses for the Cords Road flight path are summarized by the histograms in Figs. 20 and 21. As expected, the results are similar to those from the Black Mountain flight path. For the natural normalization (Fig. 20), the mean-squared error is minimized in the majority of the cases by applying all of the available power to the lower antenna (99884 or 65% for $E_b/N_0 = 10$ dB, and 92566 or 60% for $E_b/N_0 = 20$ dB). What is different here is that in those cases where this is not true, the preference is to allocate 100% to the upper antenna. This alternate

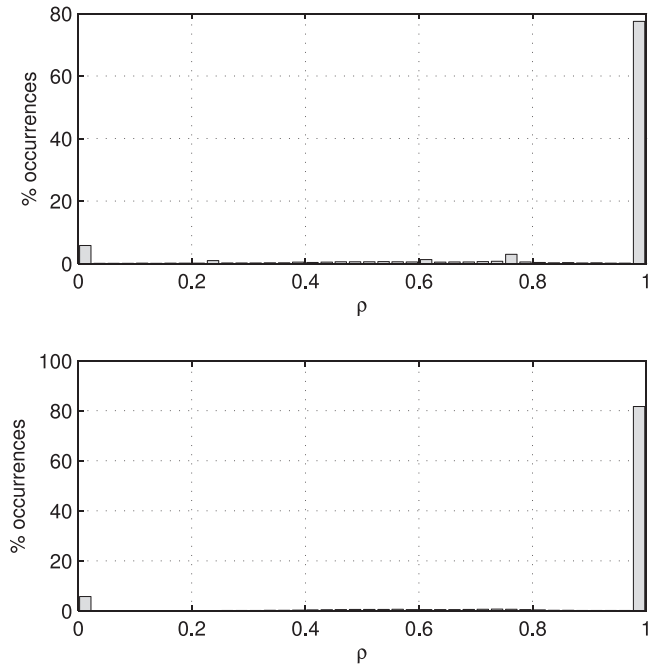


Fig. 19. Optimum power allocations for measured channel impulse responses from Black Mountain flight path at Edwards Air Force Base, California, using equal-energy normalization: (top) $E_b/N_0 = 10$ dB; (bottom) $E_b/N_0 = 20$ dB.

preference becomes less pronounced as signal-to-noise ratio increases. For the equal-energy normalization (Fig. 21), the preference reverses, and the mean-squared error is minimized by applying 100% of the available power to the upper antenna in the vast majority of the cases (116656 or 76% for $E_b/N_0 = 10$ dB, and 124985 or 81% for $E_b/N_0 = 20$ dB).

In summary, the Black Mountain and Cords Road flight paths are characterized by similar geometries. The channel between the upper antenna and the receiver, $h_1(n)$, is characterized by lower signal-to-noise ratio and lower ISI than $h_2(n)$ (the channel between the lower antenna and the receiver). Using the natural normalization, the equalizer is able to remove ISI to the point where signal-to-noise ratio is the dominant factor. In this case, applying 100% of the available energy to the lower antenna is the optimum approach in most of the cases. Using the equal-energy normalization, differences in signal-to-noise ratio are removed, so that ISI becomes the dominant factor. Because the ISI on the channel from the upper antenna is so much less than the ISI from the lower antenna, applying 100% of the available energy to the upper antenna is the optimum.

D. A Statistical Model for Triply Selective Channels

It is interesting to compare these results with what might be inferred from using a simple statistical channel model. To do so, we use a simple Gaussian model for each channel such as that used in [37]. In this experiment, channel 1 consists of 11 independent and identically distributed (IID) zero-mean complex-valued Gaussian

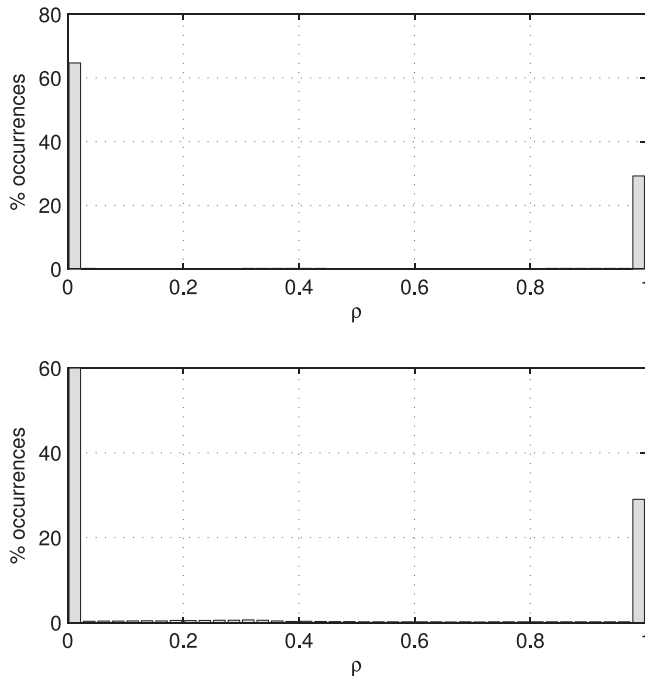


Fig. 20. Optimum power allocations for measured channel impulse responses from Cords Road flight path at Edwards Air Force Base, California, using natural normalization: (top) $E_b/N_0 = 10$ dB; (bottom) $E_b/N_0 = 20$ dB.

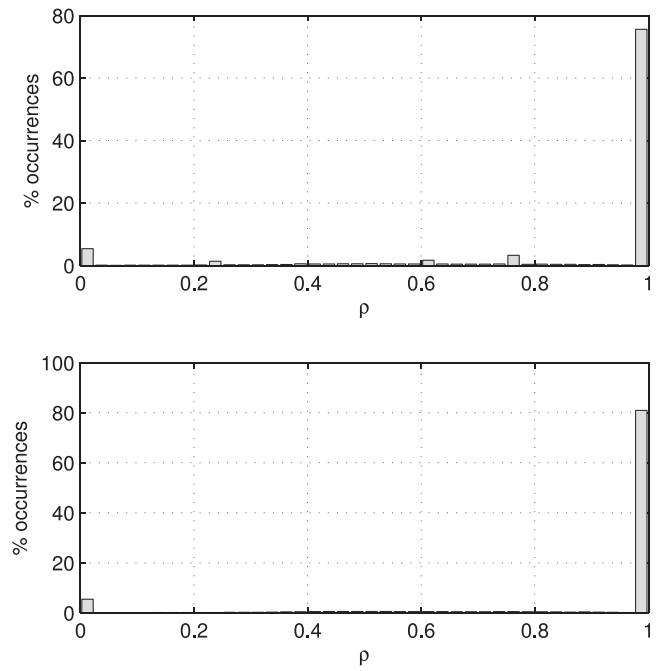


Fig. 21. Optimum power allocations for measured channel impulse responses from Cords Road flight path at Edwards Air Force Base, California, using equal-energy normalization: (top) $E_b/N_0 = 10$ dB; (bottom) $E_b/N_0 = 20$ dB.

random variables, and channel 2 consists of 18 IID zero-mean complex-valued Gaussian random variables. These numbers, 11 and 18, are the average lengths of $h_1(n)$ and $h_2(n)$, respectively, in the Cairns Army Airfield data set examined in section IVA. The channels were normalized using the equal-energy normalization described above, and 39300 independent realizations were produced. The results are summarized by the histograms in Fig. 22. The temptation is to think of the optimum ρ as a normally distributed random variable, but it should be kept in mind that this is not the case because $0 \leq \rho \leq 1$. For modest values of E_b/N_0 , we observe that the mean value of the optimum ρ is about 0.5. Given the fact that $\rho = 0.5$ corresponds to traditional TR-STBC, we see that the simple statistical model suggests that traditional TR-STBC is the best on average. This is in contrast to the conclusion drawn from the measured channel data, where a strong preference for transmit selection diversity is observed.

As E_b/N_0 increases, the optimum value of ρ appears to increase. This is explained as follows: As E_b/N_0 increases, the contribution to postequalization mean-squared error from additive noise is reduced, and ISI starts to become the dominant contributor. The optimum $\rho > 0.5$ means the system prefers to allocate more energy to channel 1 than channel 2. This makes sense because channel 1 is shorter, and this tends to contribute less residual ISI at the equalizer output.

V. DISCUSSION AND CONCLUSIONS

The expression for the postequalization mean-squared error (38) was developed by formulating a generalization

of TR-STBC that included not only transmit selection diversity and traditional TR-STBC, but also a generalization that permitted the transmitter to allocate unequal power to each transmit antenna. The concept of using postequalization mean-squared error to determine the optimum power allocation for a two-transmit, one-receive antenna system was applied to a set of measured channel impulse responses collected by sounding experiments in multipath-prone locations at Cairns Army Airfield, Ft. Rucker, Alabama, and Edwards Air Force Base, California. For each pair of channel impulse responses, the value of ρ that minimized the postequalization mean-squared error (38) was computed. The computed values for ρ were used to form histograms to summarize the results. These results illustrate the following points:

- 1) In a two-transmit, one-receive antenna system operating in a flat fading environment, if the two channels have unequal gains, the optimum power allocation applies all of the available power to the stronger channel. That is, transmit selection diversity is optimum. In contrast, in a frequency-selective fading environment, the optimum approach is to apply power to produce the best tradeoff between SNR and ISI. That is, transmit selection diversity may not be optimum. The optimum value of ρ associated with the GTR-STBC system described in this paper identifies the best tradeoff between SNR and ISI. There are some channel pairs for which $\rho = 0$ or 1 is the optimum (transmit diversity case) and some channel pairs

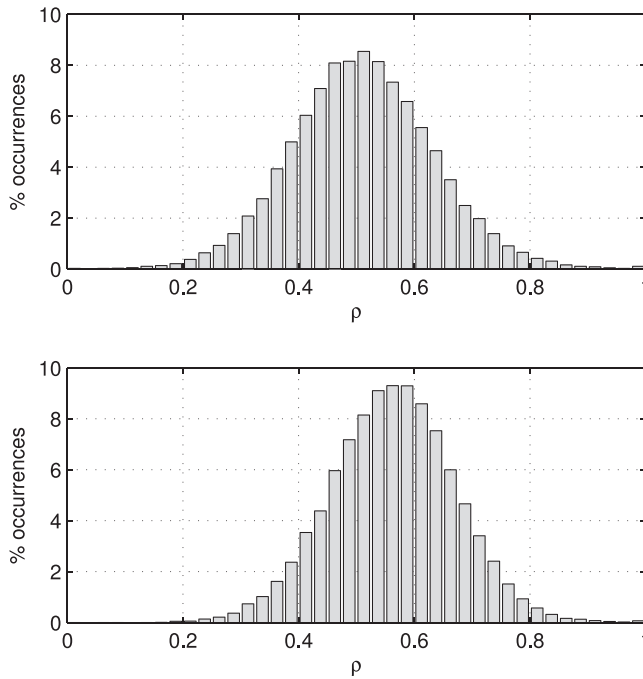


Fig. 22. Optimum power allocations for pairs of equal-energy channels where channel coefficients are IID zero-mean complex-valued Gaussian random variables: (top) $E_b/N_0 = 10$ dB; (bottom) $E_b/N_0 = 20$ dB.

for which $\rho = \frac{1}{2}$ (traditional TR-STBC) is the optimum. However, there are also many channel pairs for which neither of these is optimum.

2) On our measured channels, transmit selection diversity was the optimum more often than traditional TR-STBC.

3) On a statistical channel, such as the one used in [37], traditional TR-STBC is the best thing to do on average. This is in contrast to the results from the measured channels. Consequently, the optimum power allocation in a real setting is not predicted well by simple statistical channel models.

The development and corresponding numerical results were for the case of two transmit antennas and one receive antenna. This case is important because it is the most common scenario encountered in aeronautical telemetry. The approach can easily be extended to systems with more than two transmit antennas and more than one receive antenna by applying Linkskog's interpretation of TR-STBC in the context of the Alamouti code to the orthogonal designs described in [38].

REFERENCES

- [1] IRIG Standard 106-04: Telemetry Standards, Range Commanders Council Telemetry Group, Range Commanders Council, White Sands Missile Range, New Mexico, 2004.
<http://www.wsmr.army.mil/RCCsite/Pages/Publications.aspx>.
- [2] Rice, M., Davis, A., and Bettweiser, C. A wideband channel model for aeronautical telemetry. *IEEE Transactions on Aerospace & Electronic Systems*, **40**, 1 (Jan. 2004), 57–69.
- [3] Lei, Q., and Rice, M. Multipath channel model for over-water aeronautical telemetry. *IEEE Transactions on Aerospace and Electronic Systems*, **45**, 2 (Apr. 2009), 735–742.
- [4] Rice, M., and Jensen, M. Multipath propagation for helicopter-to-ground MIMO links. In *Proceedings of the IEEE Military Communications Conference*, Baltimore, MD, October 2011.
- [5] Rice, M., and Jensen, M. A comparison of L-band and C-band multipath propagation at Edwards AFB. In *Proceedings of the International Telemetry Conference*, Las Vegas, NV, October 2011.
- [6] Cheung, J., and Steele, R. Soft-decision feedback equalizer for continuous phase modulated signals in wideband mobile radio channels. *IEEE Transactions on Communications*, **42**, 2/3/4 (Feb./Mar./Apr. 1994), Part 3, 1628–1638.
- [7] Yiin, L., and Stuber, G. MLSE and soft-output equalization for trellis-coded continuous phase modulation. *IEEE Transactions on Communications*, **45**, 6 (Jun. 1997), 651–659.
- [8] Nguyen, H., and Levy, B. Blind and semi-blind equalization of CPM signals with the EMV algorithm. *IEEE Transactions on Signal Processing*, **51**, 10 (Oct. 2003), 2650–2664.
- [9] Özgül, B., Koca, M., and Deliç, H. Doubly iterative equalization of continuous-phase modulation. *IEEE Transactions on Communications*, **55**, 11 (Nov. 2007), 2114–2124.
- [10] Tan, J., and Stuber, G. Frequency-domain equalization for continuous phase modulation. *IEEE Transactions on Wireless Communications*, **4**, 5 (Sep. 2005), 2479–2490.
- [11] Pincaldi, F., and Vitetta, G. Equalization algorithms in the frequency domain for continuous phase modulations. *IEEE Transactions on Communications*, **54**, 4 (Apr. 2006), 648–658.
- [12] Van Thillo, W., Horlin, F., Nsenga, J., Ramon, V., Bourdoux, A., and Lauwereins, R. Low-complexity linear frequency domain equalization for continuous phase modulation. *IEEE Transactions on Wireless Communications*, **8**, 3 (Mar. 2009), 1435–1445.
- [13] Özgül, B., Koca, M., and Deliç, H. Double turbo equalization of continuous phase modulation with frequency domain processing. *IEEE Transactions on Communications*, **57**, 12 (Dec. 2009), 3579–3584.
- [14] Park, C., Heath, R., and Rappaport, T. Frequency-domain channel estimation and equalization for continuous-phase modulations with superimposed pilot sequences. *IEEE Transactions on Vehicular Technology*, **58**, 9 (Nov. 2009), 4903–4908.
- [15] Özgül, B., Koca, M., and Deliç, H. Double turbo equalization of continuous phase modulation with frequency domain processing. *IEEE Transactions on Communications*, **57**, 2 (Feb. 2009), 426–429.
- [16] Van Thillo, W., Horlin, F., Ramon, V., Bourdoux, A., and Lauwereins, R.

- Novel block constructions using an intrafix for CPM with frequency domain equalization.
IEEE Transactions on Wireless Communications, **9**, 3 (Mar. 2010), 951–955.
- [17] Saleem, S., and Stuber, G.
Linear diophantine constrained intra-fix for frequency domain equalization of multi- h CPM.
IEEE Transactions on Communications, **60**, 8 (Aug. 2012), 2265–2274.
- [18] Williams, I., and Saquib, M.
Linear frequency domain equalization of SOQPSK-TG for wideband aeronautical telemetry channels.
IEEE Transactions on Aerospace and Electronic Systems, **49**, 1 (Jan. 2013), 640–647.
- [19] Saleem, S., and Stuber, G.
Frequency-domain equalization techniques for multi- h continuous phase modulation.
IEEE Transactions on Communications, **62**, 6 (Jun. 2014), 1818–1829.
- [20] Bianchi, P., and Loubaton, P.
On the blind equalization of continuous phase modulated signals using the constant modulus criterion.
IEEE Transactions on Signal Processing, **55**, 3 (Mar. 2007), 1047–1061.
- [21] Osman, O., and Ucan, O.
Blind equalization of turbo trellis-coded partial-response continuous-phase modulation signaling over narrow-band Rician fading channels.
IEEE Transactions on Wireless Communications, **4**, 2 (Mar. 2005), 397–403.
- [22] Tse, D., and Viswanath, P.
Fundamentals of Wireless Communication. Cambridge, UK: Cambridge University Press, 2005.
- [23] Raleigh, G., and Cioffi, J.
Spatio-temporal coding for wireless communications.
IEEE Transactions on Communications, **46**, 3 (Mar. 1998), 357–366.
- [24] Alamouti, S.
A simple transmit diversity technique for wireless communications.
IEEE Journal on Selected Areas in Communications, **16**, 8 (Oct. 1998), 1451–1458.
- [25] Tarokh, V., Seshadri, N., and Calderbank, A. R.
Spacetime codes for high data rate wireless communication: Performance criterion and code construction.
IEEE Transactions on Information Theory, **44**, 2 (Mar. 1998), 744–765.
- [26] Lindskog, E., and Paulraj, A.
A transmit diversity scheme for channels with intersymbol interference.
In *Proceedings of the IEEE International Conference on Communications*, New Orleans, LA, June 2000.
- [27] Al-Dhahir, N., Naguib, A., and Calderbank, R.
Finite-length MIMO decision feedback equalization for space-time block-coded signals over multipath-fading channels.
IEEE Transactions on Vehicular Technology, **50**, 4 (Jul. 2001), 1176–1182.
- [28] Diggavi, S., Al-Dhahir, N., and Calderbank, R.
Algebraic properties of spacetime block codes in intersymbol interference multiple-access channels.
IEEE Transactions on Information Theory, **49**, 10 (Oct. 2003), 2403–2414.
- [29] Gerstacker, W., Oestermer, F., Schober, R., Lehmann, A., and Lampe, L.
Equalization concepts for Alamouti's space-time block code.
IEEE Transactions on Communications, **52**, 7 (Jul. 2004), 1178–1190.
- [30] Zhu, Y., and Letaief, K.
Single-carrier frequency-domain equalization with decision-feedback processing for time-reversal space-time block-coded systems.
IEEE Transactions on Communications, **53**, 7 (Jul. 2005), 1127–1131.
- [31] Rice, M., and Saquib, M.
MIMO equalization for helicopter-to-ground communications.
In *Proceedings of the IEEE Military Communications Conference*, Baltimore, MD, October 2011.
- [32] Perrins, E., and Rice, M.
Reduced-complexity approach to iterative detection of coded SOQPSK.
IEEE Transactions on Communications, **55**, 7 (July 2007), 1354–1362.
- [33] Nelson, T., Perrins, E., and Rice, M.
Near optimal common detection techniques for shaped offset QPSK and Feher's QPSK.
IEEE Transactions on Communications, **56**, 5 (May 2008), 724–735.
- [34] Perrins, E.
FEC systems for aeronautical telemetry.
IEEE Transactions on Aerospace and Electronic Systems, **49**, 4 (Oct. 2013), 2340–2352.
- [35] Proakis, J., and Salehi, M.
Digital Communications (5th ed.). New York: McGraw-Hill, 2007.
- [36] Treichler, J., Fijalkow, I., and Johnson, C. R.
Fractionally spaced equalizers: How long should they be?
IEEE Signal Processing Magazine, **13**, 3 (May 1996), 65–81.
- [37] Zhang, Z., Duman, T., and Kurtas, E.
Achievable information rates and coding for MIMO systems over ISI channels and frequency-selective fading channels.
IEEE Transactions on Communications, **52**, 10 (Oct. 2004), 1698–1710.
- [38] Tarokh, V., Jafarkhani, H., and Calderbank, A. R.
Space-time block codes from orthogonal designs.
IEEE Transactions on Information Theory, **45**, 5 (Jul. 1999), 1456–1467.



Michael Rice (M'82—SM'98) received a B.S.E.E. degree from Louisiana Tech University in 1987 and his Ph.D. degree from Georgia Tech in 1991. Dr. Rice was with Digital Transmission Systems, Inc., in Atlanta and joined the faculty at Brigham Young University in 1991, where he is currently the Jim Abrams Professor in the Department of Electrical & Computer Engineering. Professor Rice was a NASA/American Society for Engineering Education Summer Faculty Fellow at the Jet Propulsion Laboratory during 1994 and 1995, where he worked on land mobile satellite systems. During the 1999–2000 academic year, Professor Rice was a visiting scholar at the Communication Systems and Signal Processing Institute at San Diego State University.

Professor Rice's research interests are in the area of digital communication theory and error control coding with a special interest in applications to aeronautical telemetry and software radio design. He has been a consultant to both government and industry on telemetry-related issues and currently serves as an associate member of the Telemetry Group of the Range Commander's Council. He is a member of the Institute of Electrical and Electronics Engineers (IEEE) Communications Society and is past chair of the Communication Theory Technical Committee. He is currently the technical editor for *Command, Control and Communication Systems* and an associate editor-in-chief for *IEEE Transactions on Aerospace and Electronic Systems*.



Md. Shah Afran received the B.Sc. degree in 2011 from the Bangladesh University of Engineering & Technology, Bangladesh, in electrical engineering. He is currently a Ph.D. candidate in electrical engineering at The University of Texas at Dallas, Richardson, TX. Earlier, he worked as a software engineer at Samsung Bangladesh R&D Center, Dhaka, Bangladesh. His research interests include communications theory, diversity and equalization techniques for aeronautical telemetry, and digital communication systems.



Mohammad Saquib (SM'09) received the B.Sc. degree in 1991 from the Bangladesh University of Engineering & Technology, Bangladesh, and the M.S. and Ph.D. degrees in 1995 and 1998, respectively, from Rutgers University, New Brunswick, NJ, all in electrical engineering. He is a professor with the Electrical Engineering Department at The University of Texas at Dallas, Richardson, TX. Earlier, he worked as a member of the technical staff at Massachusetts Institute of Technology Lincoln Laboratory, and as an assistant professor at Louisiana State University, Baton Rouge, LA. His current research interests include various aspects of wireless data transmission, radio resource management, and signal processing techniques for low-cost radar applications.